arXiv:2404.01172v2 [physics.flu-dyn] 2 Apr 2024

Covering convection with thermal blankets: formation of supercontinents

Jinzi Mac Huang[1,2]†

[1]NYU-ECNU Institute of Physics and Institute of Mathematical Sciences, New York University Shanghai, Shanghai, China

[2]Applied Math Lab, Courant Institute, New York University, New York, USA

The continental plates of Earth are known to drift over a geophysical timescale, and their interactions have lead to some of the most spectacular geoformations of our planet while also causing natural disasters such as earthquakes and volcanic activity. Understanding the dynamics of interacting continental plates is thus significant. In this work, we present a fluid mechanical investigation of the plate motion, interaction, and dynamics. Through numerical experiments, we examine the coupling between a convective fluid and plates floating on top of it. With physical modeling, we show the coupling is both mechanical and thermal, leading to the thermal blanket effect: the floating plate is not only transported by the fluid flow beneath, it also prevents the heat from leaving the fluid, leading to a convective flow that further affects the plate motion. By adding several plates to such a coupled fluid-structure interaction, we also investigate how floating plates interact with each other and show that, under proper conditions, small plates can converge into a supercontinent.

1. Introduction

Fluid-structure interactions appear at many different scales on our planet, and perhaps the largest one is the continental plate tectonics (Plummer *et al.* 2001). It is believed that this tectonic motion results from the thermal convection in Earth's mantle (Kious & Tilling 1996), where the mantle materials behave like a fluid (Turcotte & Schubert 2002) that is heated from the core and cooled at the surface of Earth. Under gravity, this configuration of heating and cooling leads to thermal convection, whose circulation provides forcing to the continental plates through shearing. This is considered to be the simplest picture of plate tectonics, however many details of the plate dynamics, like the periodic formation of supercontinents and the associated geological Wilson cycle (Burke 2011), require further investigation.

Laboratory experiments have proven to be an effective way of understanding the fluid-structure interaction behind the plate tectonics, with many successful studies that couple the thermally convective fluid to solid structures (Elder 1967; Howard *et al.*
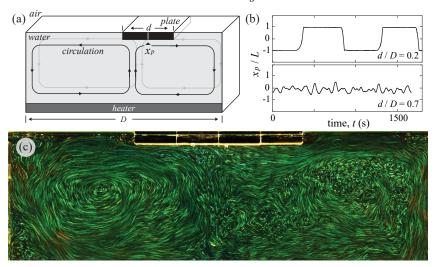
Figure 1: Rayleigh-Bénard convection coupled to a free-floating plate leads to different dynamics of plate motion. (a) Schematics of the interaction between Rayleigh-Bénard convection and the floating plate. The fluid is heated from below and has an open free surface, the floating plate on this free surface is transported by the fluid force exerted from below. (b) Different states of plate motion. A small plate with $d/D = 0.2$ oscillates between two sidewalls of the convection cell, while a big plate with $d/D = 0.7$ is trapped in the middle of the convection cell. Here $L = (D - d)/2$ is the bound of plate center x_p. (c) Flow visualization reveals two counter-rotating large-scale circulations when the plate is located at the center of the convection cell. Image credit: Zhong & Zhang (2007b); Huang et al. (2018).

1970; Whitehead 1972). Aimed at recovering the plate dynamics and understanding the associated fluid-structure interactions, a series of laboratory experiments was later conducted by Zhang & Libchaber (2000); Zhong & Zhang (2005, 2007a,b). Shown in Fig. 1(a), this experiment employs water as the working fluid, and a heater beneath provides heating while the ventilation at water-air interface provides cooling, resulting in Rayleigh-Bénard convection (Ahlers et al. 2009). A floating plate of size d is carefully placed on top of this convective domain of total length D. This moving plate with center location x_p has only fluid force acting on it, unless it hits the wall on the left or the right. Large-scale circulations (Araujo et al. 2005; Brown & Ahlers 2007; Moore & Huang 2023) are observed to form in the convective fluid, as shown in Fig. 1(a) and Fig. 1(c). Depending on the location x_p, the plate can be either transported by the circulating fluid, or situated on top of a converging or a diverging center of the surface flow [this is the case shown in Fig. 1(a)]. Interestingly, different plate motions are observed depending on its size: When the ratio between plate size d and tank width D is smaller than a critical number near 0.58, the plate oscillates between the two sidewalls as shown in Fig. 1(b); When this ratio is above the critical value, the plate is trapped at the center of tank, as shown in Fig. 1(b) and Fig. 1(c).

Zhong, Zhang, and others investigated this transition of behaviors, and they discovered that the so-called thermal blanket effect is responsible here (Zhang & Libchaber 2000; Zhong & Zhang 2005, 2007a,b; Huang et al. 2018; Mao et al. 2019; Mao 2021; Lowenstein 2024). In this theory, the floating plate serves as an insulator (like a blanket) on top of the convective fluid, hence the fluid beneath becomes warmer due to the lack of ventilation. The warm fluid then rises, creating a diverging surface flow as shown in Fig. 1(a) that can transport the plate. The coupling between the fluid and the floating plate

therefore goes two ways: the plate modifies the flow temperature and leads to thermal convection; the formed convective flows transport the floating plate. Their interplay leads to nontrivial dynamics of the plate shown in Fig. 1(b), and the physically inspired Zhong-Zhang model (Zhong & Zhang 2005, 2007a,b) successfully captures the transition of dynamics. Recently, more careful investigations on the Zhong-Zhang model have lead to new advancements in the stochastic (Huang *et al.* 2018) and dynamical (Lowenstein 2024) modeling of fluid-structure interactions.

While the laboratory experiments are conducted in a domain of fluid with finite size, numerical simulations can be conducted in a domain that resembles the mantle of Earth. The numerical work of Gurnis (1988) provides one of the first time-dependent simulations of continental drift, where the fluid domain is 2-dimensional and periodic. After this, many more numerical works have investigated the details of continental drift (Zhong & Gurnis 1993; Lowman & Jarvis 1993, 1995; Lowman & Gable 1999; Lowman & Jarvis 1999; Lowman *et al.* 2001; Zhong *et al.* 2000), engaging higher resolutions, more detailed modeling of fluid-structure interactions, and 3-dimensional simulations of the interior of Earth. In recent years, the mobility of the continental plate has become a focus of numerical study, where persistent motion is observed for larger plates while small plates tend to move sporadically (Gurnis 1988; Whitehead & Behn 2015; Mao *et al.* 2019; Mao 2021). In these works, the thermal blanket effect is once again recognized as an important factor causing the diverse plate dynamics.

This work is a continuation of an earlier investigation, Huang (2024), where the thermal and mechanical coupling between one floating plate and convective fluid is modelled through a simple stochastic model. This model shows that the covering ratio Cr, defined as the ratio of the plate area to the total surface area, is a direct measure of the thermal blanket effect. A critical covering ratio Cr^* is identified to distinguish the dynamics of the plate: For a small plate with $Cr < Cr^*$, the plate is passive to the flow field and exhibits little motion; For a plate with $Cr > Cr^*$, the strong thermal blanket effect leads to persistent plate translation.

In this work, we first introduce an efficient 2-dimensional spectral solver that can accurately capture the motions and interactions of multiple floating plates on top of Rayleigh-Bénard convection. In a periodic domain shown in Fig. 2, this solver can handle the Navier-Stokes flows presented in laboratory experiments, with simple modifications available for the geophysical Stokes flows in the mantle. Moreover, multiple floating plates can be simulated as fast as a single plate problem, as the floating plates are simply treated as an area with different boundary conditions. A specially-tailored spectral solver handles the resulting inhomogeneous Robin conditions for both the temperature and the stream function, allowing for efficient time-stepping and spectral accuracy. This enables us to systematically introduce 1, 2, and many floating plates, and to show how the thermal blanket effect dictates their interactions with the convective flow beneath and each other. The covering ratio Cr is once again identified as a key factor affecting the plate dynamics and the stable formation of supercontinents.

This paper is arranged as follows: In Section 2, we will mathematically formulate the Rayleigh-Bénard convection and its coupling to the plate motion; In Section 3, a numerical scheme and its implementation for solving this free-boundary problem will be introduced; In Section 4, numerical simulations of single, double, and multiple plate dynamics will be included and discussed; Finally, we will discuss extensions and future works in Section 5.
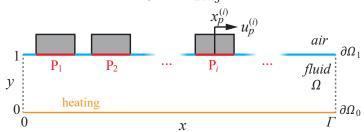
Figure 2: Schematics of the floating plate problem. The fluid domain Ω is heated from the bottom surface $\partial\Omega_0$ and has an open surface on top ($\partial\Omega_1$), floating plates $P_1, P_1, P_2, \ldots$ cover part of this open surface and shield the heat from leaving the fluid.

2. Mathematical formulation

2.1. *Flow and temperature equations*

We consider a dimensionless set of equations by rescaling the length scale by the cell height H, the time scale by the diffusion time H^2/κ (κ is thermal diffusivity), and temperature by the temperature difference ΔT between the heater and free surface. The x direction of the fluid domain is periodic with period $\Gamma = D/H$ (D is the domain width), so the overall computational domain is $x \in (0, \Gamma)$, $y \in (0, 1)$ as shown in Fig. 2. With the Boussinesq approximation, the resulting PDEs for flow speed $\boldsymbol{u} = (u, v)$, pressure p, and temperature $\theta \in [0, 1]$ are

$$\frac{D\boldsymbol{u}}{Dt} = -\nabla p + \mathrm{Pr}\,\nabla^2 \boldsymbol{u} + \mathrm{Ra}\,\mathrm{Pr}\,\theta, \tag{2.1}$$

$$\nabla \cdot \boldsymbol{u} = 0, \tag{2.2}$$

$$\frac{D\theta}{Dt} = \nabla^2 \theta. \tag{2.3}$$

Two dimensionless numbers appear during this non-dimensionalization: the Rayleigh number $\mathrm{Ra} = \alpha g \Delta T H^3 / \nu\kappa$ and the Prandtl number $\mathrm{Pr} = \nu/\kappa$, with ν, α and g denoting kinematic viscosity, thermal expansion coefficient of the fluid, and the acceleration due to gravity. We have further assumed that the physical properties of the fluid depend on temperature weakly, so Ra and Pr do not depend on θ.

As our simulation is 2-dimensional, it is convenient to write the Navier-Stokes equation in a vorticity & steam function format (Peyret 2002),

$$\frac{D\omega}{Dt} = \mathrm{Pr}\nabla^2\omega + \mathrm{PrRa}\frac{\partial\theta}{\partial x}, \tag{2.4}$$

$$-\nabla^2\psi = \omega, \quad \boldsymbol{u} = \nabla_\perp\psi, \tag{2.5}$$

$$\frac{D\theta}{Dt} = \nabla^2\theta. \tag{2.6}$$

Instead of directly solving for $\boldsymbol{u}$ and p, the z-component of vorticity $\omega = \mathbf{k} \cdot \nabla \times \boldsymbol{u}$ and the stream function defined by $\boldsymbol{u} = \nabla_\perp\psi = (\psi_y, -\psi_x)$ are solved first.

2.2. *Boundary conditions*

While Eqs. (2.4) to (2.6) are standard for modeling Rayleigh-Bénard convection, the boundary conditions become complicated when floating plates are present. Shown in Fig. 2, the fluid domain Ω is bounded between the bottom heating wall $y = 0$ ($\partial\Omega_0$) and the top free surface $y = 1$ ($\partial\Omega_1$). The segments of top surface covered by the floating plates are labelled as $P_1, P_2, \cdots$, whose centers are $x_p^{(1)}, x_p^{(2)}, \cdots$.

The boundary conditions for the bottom heating wall are set straightforwardly as constant temperature and no-slip,

$$\theta = 1, \, u = v = 0 \quad \text{at } y = 0. \tag{2.7}$$

For the vorticity-stream function format,

$$\theta = 1, \, \psi = \psi_y = 0 \quad \text{at } y = 0. \tag{2.8}$$

The top condition consists of two types of regions: for the free surface (not covered by P_i), the temperature is low and the flow is shear free; for the region covered by the plate P_i, the heat flux is zero and the flow shares the same velocity as the plate. The zero-flux condition originates from the "thermal blanket" effect caused by the low heat conduction of solids. The boundary conditions at $y = 1$ can be summarized as

$$\theta = 0, \, u_y = v = 0 \quad \text{for } y = 1 \text{ and } x \notin \cup P_i, \tag{2.9}$$

$$\theta_y = 0, \, u = u_p^{(i)}, v = 0 \quad \text{for } y = 1 \text{ and } x \in P_i. \tag{2.10}$$

Here $u_p^{(i)} = \dot{x}_p^{(i)}$ is the velocity of ith plate P_i. For convenience, we can also write the top boundary conditions in a more compact way,

$$\begin{cases} (1 - a)\,\theta + a\,\theta_y = 0 \\ a\,u + (1 - a)\,u_y = g \\ v = 0 \end{cases} \quad \text{at } y = 1. \tag{2.11}$$

For the vorticity-stream function format,

$$\begin{cases} (1 - a)\,\theta + a\,\theta_y = 0 \\ a\,\psi_y + (1 - a)\,\psi_{yy} = g \\ \psi = 0 \end{cases} \quad \text{at } y = 1. \tag{2.12}$$

Here $a(x) = \sum_i \mathbb{1}_{x \in P_i}$, $g(x) = \sum_i u_p^{(i)} \mathbb{1}_{x \in P_i}$, and $\mathbb{1}_{x \in P_i}$ is the characteristic function such that

$$\mathbb{1}_{x \in P_i} = \begin{cases} 1 & \text{if } x \in P_i, \\ 0 & \text{otherwise.} \end{cases} \tag{2.13}$$

On plate P_i, two types of forces drive its motion: the fluid force $f^{(i)}$ due to the shear from convective flows; the interacting force $f_l^{(i)}$ or $f_r^{(i)}$ when the left or right neighboring plate (P_{i-1} or P_{i+1}) makes contact with plate P_i.

For the fluid force, we simply integrate the fluid shear stress,

$$f^{(i)} = -\text{Pr} \int_{P_i} u_y(x, 1, t)\, dx = -\text{Pr} \int_0^\Gamma u_y(x, 1, t) \mathbb{1}_{x \in P_i} d\,x. \tag{2.14}$$

The interaction forces $f_l^{(i)}$ and $f_r^{(i)}$ are modelled as a short-range interaction force to ensure a fully-elastic collision between plates. The numerical implementations will be included in Section 3.6.

Finally, we add all the forces together and evolve the plate location as

$$\dot{x}_p^{(i)} = u_p^{(i)}, \tag{2.15}$$

$$\dot{u}_p^{(i)} = a_p^{(i)} = m^{-1} \left[f_l^{(i)} + f_r^{(i)} - \text{Pr} \int_0^\Gamma u_y(x, 1, t) \mathbb{1}_{x \in P_i} \, dx \right]. \tag{2.16}$$

Here $a_p^{(i)}$ is the acceleration of P_i and m is the dimensionless mass of plate.

3. Numerical methods

3.1. Time stepping

We discretize time with the second order Adam-Bashforth Backward Differentiation method (ABBD2). At time step $t_n = n\Delta T$, Eqs. (2.4) to (2.6) become

$$\nabla^2 \omega_n - \sigma_1 \omega_n = f_n, \qquad (3.1)$$

$$\nabla^2 \theta_n - \sigma_2 \theta_n = h_n, \qquad (3.2)$$

$$-\nabla^2 \psi_n = \omega_n, \qquad (3.3)$$

where

$$\sigma_1 = \frac{3}{2\,\mathrm{Pr}\,\Delta t}, \quad \sigma_2 = \frac{3}{2\Delta t}, \qquad (3.4)$$

$$f_n = \mathrm{Pr}^{-1}\left[2(\boldsymbol{u}\cdot\nabla\omega)_{n-1} - (\boldsymbol{u}\cdot\nabla\omega)_{n-2}\right] \qquad (3.5)$$

$$- (2\,\mathrm{Pr}\,\Delta t)^{-1}\left(4\omega_{n-1} - \omega_{n-2}\right) - \mathrm{Ra}\left(\frac{\partial\theta}{\partial x}\right)_n,$$

$$h_n = \left[2(\boldsymbol{u}\cdot\nabla\theta)_{n-1} - (\boldsymbol{u}\cdot\nabla\theta)_{n-2}\right] - (2\Delta t)^{-1}\left(4\theta_{n-1} - \theta_{n-2}\right). \qquad (3.6)$$

Equations (3.1) to (3.3) are Helmholtz equations that can be solved by standard numerical methods (Peyret 2002), and this implicit-explicit operator splitting scheme has been used in many numerical studies of thermal convection (Huang & Zhang 2022; Huang 2024). However, modifications have to be made to accommodate for the inhomogeneous Robin boundary conditions Eq. (2.12). We will detail this Helmholtz solver in the next few sections.

In Eqs. (3.5) and (3.6), nonlinear terms like $\boldsymbol{u}\cdot\nabla\theta$ and $\boldsymbol{u}\cdot\nabla\omega$ are computed pseudo-spectrally, with a simple and efficient anti-aliasing filter (Hou & Li 2007). With given initial and boundary data, (3.2) can be solved first to obtain θ_n, which is inserted in f_n so (3.1) can be solved next. Finally, (3.3) is solved with the known ω_n. During time stepping, we typically set $\Delta t = 5 \times 10^{-4}\,\mathrm{Ra}^{-1/2}$ considering that the flow speed $|\boldsymbol{u}| \sim \sqrt{\mathrm{Ra}}$.

After solving for the flow and temperature fields, the acceleration $a_{p,n}^{(i)}$ of plate P_i can be computed via Eq. (2.16), and Eqs. (2.15) and (2.16) are integrated with a 2nd order Adam-Bashforth method,

$$x_{p,\,n+1}^{(i)} = x_{p,\,n}^{(i)} + \frac{\Delta t}{2}\left[3u_{p,\,n}^{(i)} - u_{p,\,n-1}^{(i)}\right], \qquad (3.7)$$

$$u_{p,\,n+1}^{(i)} = u_{p,\,n}^{(i)} + \frac{\Delta t}{2}\left[3a_{p,\,n}^{(i)} - a_{p,\,n-1}^{(i)}\right]. \qquad (3.8)$$

3.2. Helmholtz solver for Dirichlet problems

Before constructing the numerical solver for Robin boundary conditions, we first outline the numerical solver for the following Helmholtz problem,

$$\nabla^2 u - \sigma u = h(x,y), \qquad (3.9)$$

$$u(x,0) = g_0(x), \qquad (3.10)$$

$$u(x,1) = g_1(x). \qquad (3.11)$$

As the domain is periodic in $x \in (0,\Gamma]$, we can discretize x as L equally-spaced nodes so $x_l = l\Delta x$ where $\Delta x = \Gamma/L$ and $l = 1,2,\ldots L$. We further require L to be odd. We can

now approximate the solution $u(x, y)$ as a truncated Fourier series in x,

$$u(x_l, y) = \sum_{k=-\frac{L-1}{2}}^{\frac{L-1}{2}} \hat{u}_k(y) \exp\left(2\pi \mathring{\imath} k l / L\right), \tag{3.12}$$

where $\mathring{\imath}$ is the imaginary unit. The Fourier coefficients $\hat{u}_k$ then satisfy the ODE,

$$\frac{d^2 \hat{u}_k}{dy^2} - \sigma_k \hat{u}_k = \hat{h}_k(y), \tag{3.13}$$

$$\hat{u}_k(0) = \hat{g}_{0,k}, \tag{3.14}$$

$$\hat{u}_k(1) = \hat{g}_{1,k}, \tag{3.15}$$

where

$$\sigma_k = \frac{4\pi^2 k^2}{\Gamma^2} + \sigma, \tag{3.16}$$

$$\hat{h}_k(y) = \frac{1}{L} \sum_{l=1}^{L} h(x_l, y) \exp\left(-2\pi \mathring{\imath} k l / L\right), \tag{3.17}$$

$$\hat{g}_{0,k} = \frac{1}{L} \sum_{l=1}^{L} g_0(x_l) \exp\left(-2\pi \mathring{\imath} k l / L\right), \tag{3.18}$$

$$\hat{g}_{1,k} = \frac{1}{L} \sum_{l=1}^{L} g_1(x_l) \exp\left(-2\pi \mathring{\imath} k l / L\right). \tag{3.19}$$

The computation of Eqs. (3.17) to (3.19) can be done efficiently with the help of the Fast Fourier Transformation (FFT) algorithm.

Now all that is left is a set of ordinary differential Eqs. (3.13) to (3.15), which can be solved with methods like finite-differences. We instead use the Chebyshev method and discretize $y \in [0, 1]$ to $M + 1$ Chebyshev nodes, so $y_m = [1 + \cos(m\pi/M)]/2$ with $m = 0, 1, 2, \ldots M$. An advantage of using the Chebyshev method is that the unevenly distributed Chebyshev nodes have a higher resolution near the boundary $y = 0$ and $y = 1$, therefore resolving the boundary layer structures. The differentiation operator $\frac{d}{dy}$ can be approximated by a discrete operator $\mathbf{D}$ (Trefethen 2000; Peyret 2002), whose elements are

$$D_{j,k} = 2\frac{c_j}{c_k}\frac{(-1)^{j+k}}{\cos(j\pi/M) - \cos(k\pi/M)} \qquad 0 \leqslant j, k \leqslant M, \ j \neq k, \tag{3.20}$$

$$D_{j,j} = -\frac{\cos(j\pi/M)}{1 - \cos^2(j\pi/M)}, \qquad 1 \leqslant j \leqslant M - 1, \tag{3.21}$$

$$D_{0,0} = -D_{M,M} = \frac{2M^2 + 1}{3}. \tag{3.22}$$

Here $c_0 = c_M = 2$, $c_j = 1$ for $1 \leqslant j \leqslant M - 1$.

The discrete operation on the LHS of Eq. (3.13) can therefore be written as

$$\mathbf{A} = \mathbf{D}^2 - \sigma_k \mathbf{I}, \tag{3.23}$$

where $\mathbf{I}$ is a $M + 1$ by $M + 1$ identity matrix.

Noticing that the Chebyshev nodes are $\mathbf{y} = [1, y_1, y_2, \ldots, y_{M-1}, 0]^\top$, we can write the discrete solution to Eqs. (3.13) to (3.15) at these locations as a column vector,

$$\mathbf{U} = [\hat{g}_{1,k}, \hat{u}_k(y_1), \hat{u}_k(y_2), \ldots, \hat{u}_k(y_{M-1}), \hat{g}_{0,k}]^\top = [\hat{g}_{1,k}, \tilde{\mathbf{U}}, \hat{g}_{0,k}]^\top. \tag{3.24}$$

The interior solution $\tilde{\mathbf{U}}$ therefore satisfies

$$\tilde{\mathbf{A}}\tilde{\mathbf{U}} = \tilde{\mathbf{H}}, \tag{3.25}$$

where the $(M-1) \times (M-1)$ matrix $\tilde{\mathbf{A}}$ is the interior of $\mathbf{A}$ (by removing its first and last rows and columns), and

$$\tilde{\mathbf{H}} = \begin{bmatrix} \hat{h}_k(y_1) - \hat{g}_{1,k}A_{1,1} - \hat{g}_{0,k}A_{1,M} \\ \hat{h}_k(y_2) - \hat{g}_{1,k}A_{2,1} - \hat{g}_{0,k}A_{2,M} \\ \vdots \\ \hat{h}_k(y_{M-1}) - \hat{g}_{1,k}A_{M-1,1} - \hat{g}_{0,k}A_{M-1,M} \end{bmatrix}. \tag{3.26}$$

Equation (3.25) is invertible, and the operator $\tilde{\mathbf{A}}$ does not change during time stepping while all the boundary information g and forcing h are contained in $\tilde{\mathbf{H}}$. This allows us to compute the LU decomposition of $\tilde{\mathbf{A}}$ at the beginning so $\tilde{\mathbf{A}}\tilde{\mathbf{U}} = \tilde{\mathbf{H}}$ can be efficiently inverted through backward and forward substitutions during time stepping. With $\tilde{\mathbf{U}}$ and $\mathbf{U}$ solved, the Fourier coefficients $\hat{u}_k$ can then be inserted into Eq. (3.12) and the solution $u(x,y)$ is therefore obtained.

3.3. *Helmholtz solver for Robin boundary conditions*

Next we consider the Helmholtz solver for equations like Eq. (3.2), where inhomogeneous Robin boundary conditions like Eq. (2.11) are applied. In a general form, consider

$$\nabla^2 u - \sigma u = h, \tag{3.27}$$
$$a_0(x)u(x,0) + b_0(x)u_y(x,0) = g_0(x), \tag{3.28}$$
$$a_1(x)u(x,1) + b_1(x)u_y(x,1) = g_1(x). \tag{3.29}$$

The idea of solving these equations is to use the influence matrix method (Peyret 2002): A PDE with inhomogeneous Robin boundary conditions can be converted into a series of PDEs with homogeneous Dirichlet boundary conditions, which can be solved by the method detailed in Section 3.2.

We first separate the solution into several subproblems, so

$$u(x,y) = \tilde{u}(x,y) + \sum_{l=1}^{2L} \xi_l \bar{u}_l(x,y), \tag{3.30}$$

where ξ_l are unknown coefficients to be determined later and

$$\nabla^2 \tilde{u} - \sigma \tilde{u} = h, \tag{3.31}$$
$$\tilde{u}(x,0) = \tilde{u}(x,1) = 0, \tag{3.32}$$

$$\nabla^2 \bar{u}_l - \sigma \bar{u}_l = 0, \tag{3.33}$$
$$\bar{u}_l|_{\eta_m} = \delta_{lm} \text{ for all } \eta_m \in \partial\Omega. \tag{3.34}$$

Here η_m represents the mth node on the boundary, so there are $2L$ of them, and δ_{lm} is the Kronecker delta function. Now, the boundary conditions Eqs. (3.28) and (3.29) indicate

$$\left[a_i(x) \left(\sum_{l=1}^{2L} \xi_l \bar{u}_l \right) + b_i(x) \left(\frac{\partial \tilde{u}}{\partial y} + \sum_{l=1}^{2L} \xi_l \frac{\partial \bar{u}_l}{\partial y} \right) - g_i(x) \right] \bigg|_{\eta_m} = 0 \text{ for } \eta_m \in \partial\Omega_i. \tag{3.35}$$

Here $i \in \{0,1\}$ indicates the bottom or top boundary. As Eq. (3.35) holds on all the

boundary nodes η_m, it provides $2L$ equations for $2L$ unknowns ξ_l, and such a linear system is invertible. With all ξ_l solved, the solution of Eqs. (3.27) to (3.29) can be recovered as $u = \tilde{u} + \sum_{l=1}^{2L} \xi_l \bar{u}_l$.

In fact, ξ_m is exactly the Dirichlet data for u at boundary node η_m, therefore the solution of Eqs. (3.27) to (3.29) is the same as the solution of

$$\nabla^2 u - \sigma u = h, \tag{3.36}$$

$$u|_{\eta_m} = \xi_m \text{ for } \eta_m \in \partial\Omega. \tag{3.37}$$

This method can directly solve the heat Eq. (3.2) with boundary conditions in Eqs. (2.8) and (2.12), by assigning $a_0 = 1$, $b_0 = 0$, $g_0 = 1$ at the bottom and $a_1 = 1 - a$, $b_1 = a$, $g_1 = 0$ at the top. Usually, the solutions of Eqs. (3.33) and (3.34) are obtained and saved at the beginning. At each time step, Eqs. (3.31) and (3.32) are solved and the location of moving plates will determine $a_i(x)$, $b_i(x)$, and $g_i(x)$, so Eq. (3.35) can be inverted to provide ξ_m which can be used as boundary data in Eqs. (3.36) and (3.37), and the solution θ_n can therefore be determined.

3.4. *Flow solver with Robin boundary conditions*

With the heat Eq. (3.2) solved, the only missing part is the following flow problem at time step n,

$$\nabla^2 \omega - \sigma\omega = f, \tag{3.38}$$

$$-\nabla^2 \psi = \omega, \tag{3.39}$$

$$\psi = \psi_y = 0 \qquad \text{at } y = 0, \tag{3.40}$$

$$\psi = 0, \quad a\,\psi_y + (1-a)\,\psi_{yy} = g \qquad \text{at } y = 1. \tag{3.41}$$

Here we have dropped all the subscripts. We can also solve these equations with the influence matrix method. Now we want to convert the Neumann boundary condition in Eq. (3.40) and Robin boundary condition in Eq. (3.41) to a Dirichlet boundary condition for vorticity ω. We decompose ω and ψ as,

$$\omega(x, y) = \tilde{\omega}(x, y) + \sum_{l=1}^{2L} \xi_l \bar{\omega}_l(x, y), \tag{3.42}$$

$$\psi(x, y) = \tilde{\psi}(x, y) + \sum_{l=1}^{2L} \xi_l \bar{\psi}_l(x, y). \tag{3.43}$$

The associated subproblems are

$$\nabla^2 \tilde{\omega} - \sigma\tilde{\omega} = f, \quad -\nabla^2 \tilde{\psi} = \tilde{\omega} \tag{3.44}$$

$$\tilde{\omega}(x, 0) = \tilde{\omega}(x, 1) = \tilde{\psi}(x, 0) = \tilde{\psi}(x, 1) = 0 \tag{3.45}$$

$$\nabla^2 \bar{\omega}_l - \sigma\bar{\omega}_l = 0, \quad -\nabla^2 \bar{\psi}_l = \bar{\omega}_l \tag{3.46}$$

$$\bar{\psi}_l(x, 1) = 0, \quad \bar{\omega}_l|_{\eta_m} = \delta_{lm} \text{ for all } \eta_m \in \partial\Omega. \tag{3.47}$$

The Neumann boundary condition in Eq. (3.40) and the Robin boundary condition in

Eq. (3.41) can now be enforced as

$$\left(\frac{\partial \tilde{\psi}}{\partial y} + \sum_{l=1}^{2L} \xi_l \frac{\partial \bar{\psi}_l}{\partial y}\right)\Bigg|_{\eta_m} = 0 \text{ for } \eta_m \in \partial\Omega_0,$$

(3.48)

$$\left[a\left(\frac{\partial \tilde{\psi}}{\partial y} + \sum_{l=1}^{2L} \xi_l \frac{\partial \bar{\psi}_l}{\partial y}\right) + (1-a)\left(\frac{\partial^2 \tilde{\psi}}{\partial y^2} + \sum_{l=1}^{2L} \xi_l \frac{\partial^2 \bar{\psi}_l}{\partial y^2}\right) - g\right]\Bigg|_{\eta_m} = 0 \text{ for } \eta_m \in \partial\Omega_1.$$

(3.49)

Equations (3.48) and (3.49) are again $2L$ equations for $2L$ unknowns ξ_l and the linear system is invertible. Equations (3.42) and (3.43) can then be summed and the solutions are obtained. In fact, ξ_l is exactly the boundary data for ω at boundary node η_l, so we can instead solve

$$\nabla^2 \omega - \sigma\omega = f,$$

(3.50)

$$-\nabla^2 \psi = \omega,$$

(3.51)

$$\psi|_{\eta_m} = 0, \ \omega|_{\eta_m} = \xi_m \text{ for } \eta_m \in \partial\Omega.$$

(3.52)

3.5. *Smooth boundary conditions*

In principle, the introduced fluid and heat solver is able to manage the inhomogeneous Robin boundary condition Eq. (2.11) at $y = 1$. However this boundary condition is not smooth, therefore limiting the accuracy of a numerical method with finite resolution. To overcome this, we aim to construct a smooth characteristic function $\hat{\mathbb{1}}_{x \in P_i}$ so it is compactly supported and sufficiently smooth.

We first construct a smooth step function in 1D, whose derivative $\phi_{l,m}(r)$ is in the family of Wendland functions that are shaped like a Gaussian (Chernih *et al.* 2014):

$$\phi_{l,m}(r) = \begin{cases} \frac{1}{\Gamma(m)2^{m-1}} \int_r^1 s(1-s)^l(s^2-r^2)^{m-1}ds & \text{for } 0 \leqslant r \leqslant 1, \\ 0 & \text{for } r > 1. \end{cases}$$

(3.53)

The integer m controls the smoothness of the Wendland function, and $l = \lfloor m + n/2 \rfloor + 1$ for spatial dimension n. It can be shown that $\phi_{l,m} \in C^{2m}(\mathbb{R}^+)$ and it is compactly supported. Next, we take $m = 1$, $l = 2$ and construct a smooth step function $W_\epsilon(x)$ that transitions from 0 to 1 on $[-\epsilon, \epsilon]$,

$$W_\epsilon(x) = \frac{\int_{-\infty}^x \phi_{2,1}(|s|/\epsilon)ds}{\int_{-\infty}^\infty \phi_{2,1}(|s|/\epsilon)ds}.$$

(3.54)

This function is plotted in Fig. 3(a) with various ϵ, and it is easy to verify that $W_\epsilon(x) = 0$ when $x < -\epsilon$ and $W_\epsilon(x) = 1$ when $x > \epsilon$. As the transition length 2ϵ becomes smaller, W_ϵ becomes sharper, approximating a step function. Moreover, $W_\epsilon \in C^3(\mathbb{R})$ when $\epsilon > 0$ due to our choice of $m = 1$, achieving our goal of constructing a smooth step function.

We can further evaluate $W_\epsilon(x)$ as

$$W_\epsilon(x) = \begin{cases} 0 & \text{if } x < -\epsilon, \\ -\frac{3}{4}\left(\frac{x}{\epsilon}\right)^5 + \frac{5}{2}\left(\frac{x}{\epsilon}\right)^4 \text{sgn}(x) - \frac{5}{2}\left(\frac{x}{\epsilon}\right)^3 + \frac{5}{4}\frac{x}{\epsilon} + \frac{1}{2} & \text{if } x \in [-\epsilon, \epsilon], \\ 1 & \text{if } x > \epsilon. \end{cases}$$

We next construct a smooth characteristic function $\hat{\mathbb{1}}_{x \in P}$ for a plate P centered at x_p
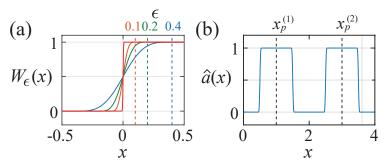
Figure 3: Smooth step and indicator functions. (a) Smooth step function W_ϵ that has a transition interval of $[-\epsilon, \epsilon]$. Four values of $\epsilon = 0.01, 0.1, 0.2, 0.4$ are plotted. (b) Smooth indicator function $\hat{a}$ for locating the region of solid plates. The parameters plotted are $x_p^{(1)} = 1$, $x_p^{(2)} = 3$, $d = 1$, and $\epsilon = 0.05$.

with length d,

$$\hat{\mathbb{1}}_{x \in P_i} = W_\epsilon \left(x - (x_p - \frac{d}{2}) \right) W_\epsilon \left((x_p + \frac{d}{2}) - x \right). \tag{3.55}$$

In our numerical examples, we take $\epsilon = 0.05d$ to ensure smoothness. Finally, we can write the Robin boundary conditions in the following form.

$$\begin{cases} (1 - \hat{a})\, \theta + \hat{a}\, \theta_y = 0 \\ \hat{a}\, u + (1 - \hat{a})\, u_y = \hat{g} \qquad \text{at } y = 1, \\ v = 0 \end{cases} \tag{3.56}$$

where

$$\hat{a}(x) = \sum_i \hat{\mathbb{1}}_{x \in P_i}, \ \hat{g}(x) = \sum_i u_p^{(i)} \hat{\mathbb{1}}_{x \in P_i}. \tag{3.57}$$

Noticing that $W_\epsilon(0) = 0.5$, it can be easily verified that $\hat{a}(x) \in [0, 1]$ as long as $|x_p^{(i)} - x_p^{(j)}| \geqslant d$ for $i \neq j$. The function $\hat{a}(x)$ for two plates centered at $x_p^{(1)} = 1$, $x_p^{(2)} = 3$ with plate length $d = 1$ is shown in Fig. 3(b).

3.6. *Dynamics of the moving plate*

There are two types of forcing on each plate. One is the fluid force due to shear stress, the other is the interaction force when two plates make contact.

For the fluid force, we simply integrate the shear stress by replacing the characteristic function with its smooth version,

$$f^{(i)} = -\mathrm{Pr} \int_0^\Gamma u_y(x, 1, t) \hat{\mathbb{1}}_{x \in P_i} d\, x = -\mathrm{Pr}\Gamma \langle u_y \hat{\mathbb{1}}_{x \in P_i} \rangle. \tag{3.58}$$

As we are using an equally spaced periodic grid in x, the integration can be replaced with a numerical average of all grid values of the integrand so $\int_0^\Gamma f(x)\, dx \approx \Gamma \langle f \rangle = (\Gamma/L) \sum_{k=1}^L f_k$, which is spectrally accurate (Trefethen 2000). When solid plates make contact, a contact force between them keeps the plates separated. Numerically, we approximate this force such that it is short-ranged and stays smooth until two plates are too close to each other. For plate number i, there are two

forces for contact from the left neighbor and from the right neighbor,

$$f_l^{(i)} = f_{\max} W_\delta \left(d - |x_p^{(i)} - x_p^{(i-1)}| \right), \tag{3.59}$$

$$f_r^{(i)} = -f_{\max} W_\delta \left(d - |x_p^{(i+1)} - x_p^{(i)}| \right). \tag{3.60}$$

Here the parameter δ models an "interaction length", and $f_{\max}$ is the maximum interacting force between two plates. At each simulation, δ and $f_{\max}$ are chosen according to the spatial and temporal resolution, so the ODE and PDE solvers can sufficiently resolve the plate motion and the associated boundary conditions. We note that this choice of interacting force conserves both the total momentum and kinetic energy of plates when fluid force is not present.

3.7. *Summary of numerical methods*

There are two stages during our numerical simulation and below we list some of the key steps during each stage.

Preprocessing stage:

(i) The inverse $\tilde{\mathbf{A}}^{-1}$ (or the LU decomposition of $\tilde{\mathbf{A}}$) in Eq. (3.25) is prepared for operators in Eqs. (3.1) to (3.3), by taking $\sigma = 0, \sigma_1, \sigma_2$ in Eq. (3.23);

(ii) Subproblems Eqs. (3.33), (3.34), (3.46) and (3.47) are solved, and the solutions $\bar{\theta}_l$, $\bar{\omega}_l$, and $\bar{\psi}_l$ for $l = 1, 2, \ldots, 2L$ are saved.

At the nth step of the time-stepping stage:

(i) The fluid and interaction forces on each plate are computed according to Eqs. (3.58) to (3.60);

(ii) The location and velocity of each plate are evolved by Eqs. (3.7) and (3.8), and the indicator function $\hat{a}$ is prepared by Eq. (3.57);

(iii) The forcing term h_n in Eq. (3.2) is prepared according to Eq. (3.6), and $\tilde{\theta}_l$ is solved from Eqs. (3.31) and (3.32);

(iv) Equation (3.35) is inverted so the Dirichlet boundary data for θ_n is known, Eqs. (3.36) and (3.37) are then solved for θ_n;

(v) The temperature θ_n is used to prepare f_n according to Eq. (3.5), so $\tilde{\omega}_l$, $\tilde{\psi}_l$ can be solved from Eqs. (3.44) and (3.45);

(vi) Equations (3.48) and (3.49) are inverted so the Dirichlet data for ω_n is known, Eqs. (3.51) and (3.52) are finally solved to provide ω_n and ψ_n.

4. Results

4.1. *One plate dynamics*

In this section, we review the dynamics of a single plate motion. To simplify our study, the Rayleigh number is fixed at Ra $= 10^6$, the Prandtl number is Pr $= 7.9$, and the aspect ratio is $\Gamma = 4$. These parameters are similar to previous numerical study (Huang 2024). For the plate, we set the mass as $m = 4d$, so plates with various length d have the same density. For the numerical solver, there are 512 Fourier modes in the x direction and 129 Chebyshev nodes in the y direction, and the time step size is $\Delta t = 10^{-6}$. These parameters yield accurate, stable, and resolved numerical solutions.

To measure the size of the plate, we define the covering ratio $Cr = d/\Gamma$. Depending on the size of the plate, or Cr, the dynamics of the plate motion can be very different.
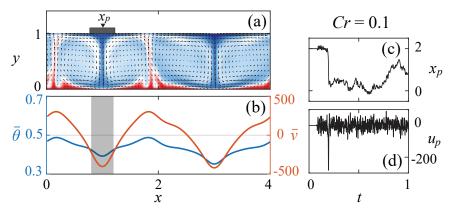
Figure 4: Motion of a small plate ($Cr = 0.1$) is random and bidirectional. (a) A snapshot of flow and temperature fields beneath a plate. The small plate is trapped at a cool converging center. (b) Vertically averaged temperature $\bar{\theta}$ and vertical velocity $\bar{v}$ at the same moment of (a). The shaded region indicates the location of the plate. At the converging center, the averaged temperature is low and the flow moves downward. (c)-(d) The displacement x_p and velocity u_p of the plate show behavior of a random walk with jumps.

Figure 4 and Supplemental Movie 1 show the dynamics of a small plate with $Cr = 0.1$, and its motion is a continuous random walk shown in Fig. 4(c). However in Fig. 5 and Supplemental Movie 2, a larger plate with $Cr = 0.6$ shows completely different dynamics: it translates unidirectionally as shown in Fig. 5(c).

In Huang (2024), the two dynamics are analyzed in detail, and we summarize the key interplay between the plate and the fluid below.

In Fig. 4, the small plate tends to be attracted by the converging center of the fluid – the location where the fluid sinks. This converging center can be clearly seen in Fig. 4(a)-(b), located at the minimum of both the vertically averaged temperature $\bar{\theta}(x,t) = \int_0^1 \theta(x,y,t)\,dy$, and the averaged vertical flow speed $\bar{v}(x,t) = \int_0^1 v(x,y,t)\,dy$. This means the plate velocity $u_p = \dot{x}_p$ in Fig. 4(d) matches the translational velocity of the flow converging center, which has a 0 mean but is subject to noise due to random fluid forcing. In this case, the plate motion is passive and completely driven by the flow structure, and the converging center of the surface flow serves as a stable equilibrium location for the plate.

For a larger plate with $Cr = 0.6$, Fig. 5 and Supplementary Movie 2 show that the plate motion becomes unidirectional. Increasing plate size clearly changes the flow and temperature distribution in the fluid, as the bulk fluid temperature in Fig. 5(a)-(b) is visibly higher than that in Fig. 4(a)-(b). This is a clear sign of the thermal blanket effect, as the bigger plate shields the heat from escaping and the effective cooling area at $y = 1$ is smaller. In this case, the plate is no longer passive, but creates a thermal blanket that warms the fluid beneath it. Unlike the situation of small plates, a large plate sitting on top of a converging center cannot be stable in the long term, as eventually the temperature beneath the plate will become high enough to turn this converging center into a divergent one. Shown in Fig. 5(b), the average temperature $\bar{\theta}$ is indeed higher below the plate, and the plate sits between the converging and diverging centers. This causes the unidirectional motion of the plate, and as the plate keeps affecting the temperature distribution beneath it, the temperature and flow fields move with the plate as shown in Supplementary Movie 2. The plate displacement x_p and velocity u_p are shown in
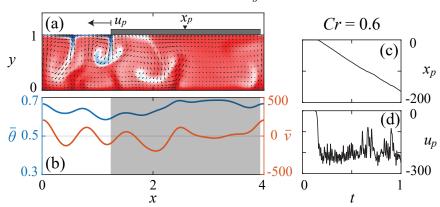
Figure 5: Motion of a large plate ($Cr = 0.6$) is unidirectional. (a)-(b) Flow and temperature fields beneath the plate. (c)-(d) The displacement x_p and velocity u_p of the moving plate, which shows a unidirectional motion with nonzero mean velocity.
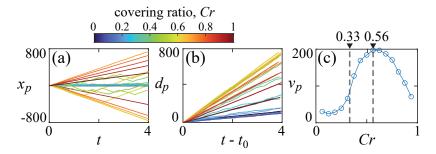

Figure 6: Plate displacement and velocity for different covering ratios Cr. (a) Sample trajectories of the plate location, where small plates are more affected by noise and large plates have more persistent unidirectional motion. (b) Total travel of the plate reveals its speed, a maximum speed of travel can be seen at around $Cr = 0.6$. (c) Average travel speed has a maximum at $Cr = 0.56$, and unidirectional motions start to appear for plates larger than $Cr = 0.33$.

Fig. 5(c)-(d), where u_p has a nonzero mean and is subject to random forcing from the fluid.

The motions of plates with various Cr are shown in Fig. 6. The displacement in Fig. 6(a) clearly shows that the small plate has a random motion whose net displacement grows slowly in time. As Cr increases, the plate starts to have more persistent unidirectional motions, however the random fluid forcing can easily reverse the travel direction of the plate, leading to reversals of direction in Fig. 6(a). Further increasing Cr, the unidirectional motion becomes more persistent, however the velocity (slope of x_p) decreases. Defining the total travel of a plate as $d_p(t) = \int_0^t |u_p(t')| \, dt'$, Fig. 6(b) shows a peak of the plate traveling speed at around $Cr = 0.6$. To further verify this, we define the average plate speed as $v_p = \lim_{t\to\infty} d_p(t)/t$ in Fig. 6(c), and a maximum indeed appears at $Cr = 0.6$.

As the thermal blanket effect strengthens, there is an apparent transition of the plate dynamics. Figure 7 shows the time series (lower panels) and histogram (upper panels) of u_p at various Cr. For small Cr, the histogram of plate velocity resembles a Gaussian distribution, whose zero mean suggests that the net plate displacement would be small. Increasing Cr beyond 0.3, the plate dynamics start to transition as Fig. 7(c) shows the variance of u_p increases. At $Cr = 0.4375$ [Fig. 7(d)], the two translational states with
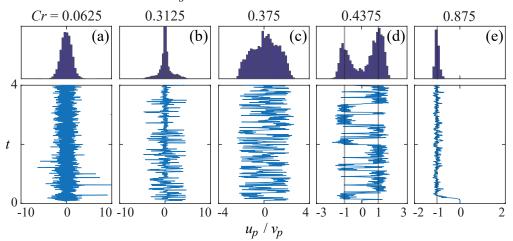
Figure 7: Time series (lower panels) and histogram (upper panels) of the plate velocity u_p at various Cr. The plate velocity is normalized by its average travel speed v_p, so $u_p \approx \pm v_p$ suggests a unidirectional translation. (a)-(e) have the covering ratio of 0.0625, 0.3125, 0.375, 0.4375, 0.875. The plate motion has a transition from the passive state (a)-(b) to the translating state (d)-(e), and the translation is also more persistent for large Cr in (e).
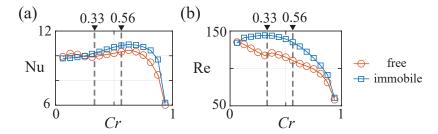

Figure 8: Nusselt and Reynolds numbers for the convecting flow. (a) The Nusselt number is a measure of the vertical heat passing through the flow. (b) Reynolds number as a measure of flow speed. The free data are for the plate freely moving with the flow, and the immobile data are for the plate that is fixed.

$u_p = \pm v_p$ emerge, where u_p switches between the two directions due to the noise of fluid forcing. At even higher Cr [Fig. 7(e)], the unidirectional motion is persistent and the reversal becomes rare. The observation here matches the stochastic theory developed in Huang (2024), which consists of a simple model that recovers the mechanical and thermal interplay between the plate and the fluid. This stochastic model predicts that there is only a passive state (no net plate motion) for $Cr < Cr^*$ where the critical covering ratio is $Cr^* = 1/3$ for $\Gamma = 4$, and the translational states can only exist for plates with $Cr > Cr^*$, indeed matching Fig. 7.

Finally, we investigate how the bulk properties of the flow respond to the moving plate. In Fig. 8, we show the Nusselt number $\text{Nu} = -[\Gamma(t_2 - t_1)]^{-1} \int_{t_1}^{t_2} dt \int_0^\Gamma \theta_y(x, 0, t)\, dx$, and Reynolds number $\text{Re} = (t_2 - t_1)^{-1} \int_{t_1}^{t_2} \left(\max_{(x,y)} |\boldsymbol{u}(x, y, t)| \right) dt$, where $t_2 - t_1$ is the interval for long-time average. The two groups of measurements are for a plate that is free to move by the flow (free), and for a plate that is fixed at a certain location (immobile). By setting the plate free, the Nusselt number decreases slightly, and this is possibly due to the moving plate effectively shielding a larger portion of the free surface. With a stronger shielding effect, the vertical heat transfer measured by the Nusselt number decreases. The
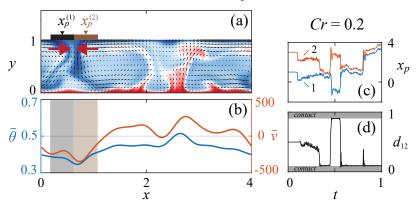
Figure 9: Dynamics of two small plates ($Cr_p = 0.1$ each) forming a supercontinent of $Cr = 0.2$. (a) Flow and temperature distribution beneath the supercontinent. The surface flow is converging and the formation of the supercontinent is stable. (b) Vertically averaged temperature $\bar{\theta}$ and vertical velocity $\bar{v}$ at the same moment of (a), with the region of the two plates shaded. (c) The displacement of plate $x_p^{(1)}$ and $x_p^{(2)}$. (d) The normalized plate distance $d_{12} = [x_p^{(2)} - x_p^{(1)}]/\Gamma$ indicates the two plates tend to stay in contact. The white region (plates separated) and gray region (plates in contact) are separated by Cr_p and $1 - Cr_p$.

flow speed, on the other hand, is seen to decrease once we let the plate move freely. This can either be caused by the increased shielding of the free surface, or be a consequence of the flow passing its kinetic energy to the moving plate. We also note at the critical Cr^*, the flow speed reaches a maximum for the immobile plate shown in Fig. 8(b), and the Nusselt number approaches its maximum at around $Cr = 0.6$ where the plate translates the fastest as shown in Fig. 6(c).

4.2. *Two-plate interactions*

Adding multiple plates to the convective surface brings interactions between plates and leads to more diverse dynamics. In our numerical simulation, adding a second plate can easily be achieved through the indicator function method outlined in Sections 2 and 3. In the following numerical experiments, we set $Ra = 10^6$, $Pr = 7.9$, $\Gamma = 4$, $m = 4d$ as we did for the single plate case. We additionally set the maximum interaction force $f_{max} = 10^6$ and an interaction range $\delta = \epsilon$ that matches the size of smoothing region of the indicator function in Section 3.5. These two parameters define the force of interaction between the two plates through Eqs. (3.59) and (3.60), and such interaction conserves both the kinetic energy and momentum of the plates.

The dynamics of a pair of small plates (Fig. 9) and a pair of large plates (Fig. 10) are quite different. In Fig. 9 and Supplementary Movie 3, two small plates with individual covering ratios $Cr_p = 0.1$ are released on the convective surface. The two plates tend to stay together, generating a "supercontinent" as shown in Fig. 9(a). Further analyzing the flow temperature and surface flow rate in Fig. 9(b), we see they are in fact attracted by a converging center of the surface flow, and the surface flow pushes them into each other. The trajectories $x_p^{(1)}$ and $x_p^{(2)}$ of the plates are shown in Fig. 9(c), and the normalized plate distance $d_{12} = [x_p^{(2)} - x_p^{(1)}]/\Gamma$ is plotted in Fig. 9(d). We clearly see that the two plates prefer to stay in contact, as the normalized distance stays near Cr_p or $1 - Cr_p$ in Fig. 9(d).

The combined covering ratio of these two plates is $Cr = 2Cr_p = 0.2$, less than the critical covering ratio of $Cr^* = 1/3$ we identified earlier. Therefore the thermal blanket
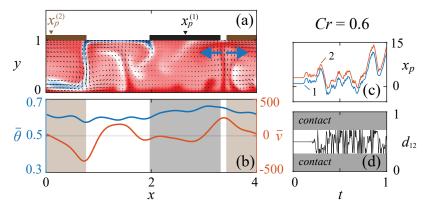
Figure 10: Two large plates ($Cr_p = 0.3$ each) cannot form a stable supercontinent of $Cr = 2Cr_p = 0.6$. (a) The warm upwelling fluid creates a diverging surface flow beneath the plates. This diverging surface flow pulls the two plates apart, rendering the supercontinent formation unstable. (b) Vertically averaged temperature and vertical velocity of the fluid beneath the plates shown in (a). (c) Plate displacement $x_p^{(1)}$ and $x_p^{(2)}$. (d) The normalized plate distance d_{12} stays in the white region where the two plates are separated.
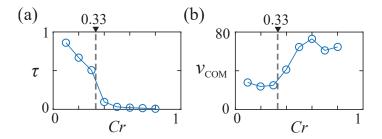

Figure 11: Contact and motion of the plates depend on the covering ratio. (a) The normalized contact time τ decreases sharply when Cr increases above $Cr^* = 1/3$. (b) The plate center of mass velocity v_{COM} increases when $Cr > Cr^*$, indicating the plates are no longer passive to the flow.

effect generated by this supercontinent is not strong enough to heat up the fluid beneath, and the surface flow stays converging and pushing the two plates together. Thus, a supercontinent with combined $Cr < Cr^*$ is stable in its formation and exhibits a passive motion.

Figure 10 and Supplementary Movie 4 show the dynamics of two plates with $Cr = 2Cr_p = 0.6$. In this case, the fluid beneath the supercontinent is warmed up due to the thermal blanket effect and generates an upwelling flow. The resulting diverging surface flow separates the two plates, leading to an unstable supercontinent formation. Figure 10(c)-(d) show the plate trajectories and the normalized plate distance, and the two plates are seen to stay separated in Fig. 10(d) as their normalized distance is in between Cr_p and $1 - Cr_p$ and the contact sate is only transient.

In Fig. 10, although the covering ratio for each plate $Cr_p < Cr^*$, their combined $Cr = 2Cr_p > Cr^*$. The supercontinent, once formed, will become unstable as the warm fluid beneath creates a diverging surface flow that pulls the two plates apart.

We now see the role of Cr^* in the formation of supercontinents: It is only possible to have a stable supercontinent if its Cr is less than Cr^*.

Figure 11 shows how the plate dynamics depend on the combined Cr. In Fig. 11(a),
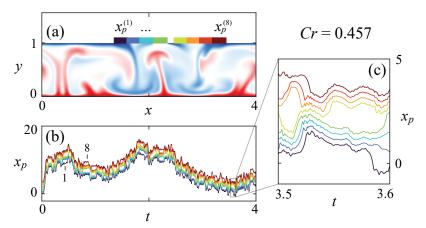
Figure 12: Dynamics of 8 plates ($Cr_p = 0.057$, $Cr = 8Cr_p = 0.457$) floating on top of the convecting fluid. (a) A snapshot of 8 plates and the convective fluid beneath, the center location of the plates are ($x_p^{(1)}, x_p^{(2)}, \cdots, x_p^{(8)}$). (b) Trajectories of ($x_p^{(1)}, x_p^{(2)}, \cdots, x_p^{(8)}$), and plates can be seen forming supercontinents over time. (c) Zoomed-in view of the trajectories in (b) in the time window of $t \in (0.35, 0.36)$.

we define a normalized contact time $\tau = t_c/T$, where t_c is the amount of time that the two plates are in contact and T is the total simulation time. A sharp decrease of τ is seen near $Cr^* = 1/3$, beyond which a persistent formation of supercontinent is unlikely. This is consistent with our analysis earlier, as a supercontinent with $Cr > Cr^*$ would induce warm upwelling flows that disintegrate the supercontinent. The center of mass (CoM) velocity of plates also picks up when $Cr > Cr^*$ [Fig. 11(b)], suggesting the two large plates are no longer passive but instead translate like we have seen in Fig. 6(c).

4.3. Multiple plates

Further increasing the number of plates, the formation of supercontinents exhibits complex and intriguing dynamics. In Fig. 12 and Supplementary Movie 4, 8 plates with $Cr_p = 0.057$ (total $Cr = 0.457$) are released on top of the convective fluid, where Ra $= 10^6$, Pr $= 7.9$, $\Gamma = 4$, $m = 4d$. The plate maximum interaction force $f_{\max} = 10^6$ and interaction range $\delta = \epsilon$ are the same as before.

Figure 12(a) shows a moment when the 8 plates form 2 supercontinents, with each supercontinent covering $4Cr_p = 0.23$ of the free surface. Each supercontinent thus has a covering ratio less than $Cr^* = 1/3$ and is thereby stable by our earlier argument. Indeed, the stable formation of a supercontinent of 4 plates can be seen on the plate trajectory ($x_p^{(1)}, x_p^{(2)}, \cdots, x_p^{(8)}$) shown in Fig. 12(b), whose zoomed-in view between $t \in (0.35, 0.36)$ is shown in Fig. 12(c). Of course, the formation of a supercontinent with a different number of plates is possible, and our theory predicts that they are stable if the number of plates $I < Cr^*/Cr_p \approx 6$.

To further analyze the formation of supercontinents, we define the formation number $I(t)$ as the number of plates forming the largest supercontinent at any given time t. A schematic of such a formation number is shown in Fig. 13(a), where 5 continents are formed and the largest supercontinent has $I = 4$. The formation number can be tracked over time, and Fig. 13(b) shows the formation number of the simulation presented in Fig. 12, with the zoomed-in view of $I(t)$ in the window of Fig. 12(c) shown in Fig. 13(c). We note that the formation number can actually take on all integer values between 1
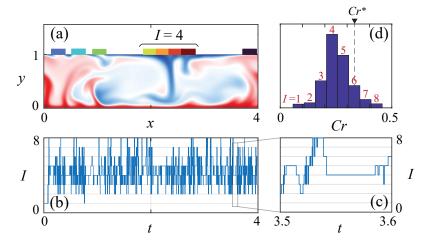
Figure 13: Statistics of the formation number $I(t)$ that is the maximum number of plates in a supercontinent at time t. (a) Schematic of $I = 4$. (b) Time series of $I(t)$ shows the possibility of forming supercontinents with various sizes. (c) Zoomed-in view of $I(t)$ in (b) during $t \in (0.35, 0.36)$. (d) Histogram of $I(t)$ indicates $I = 4$ is the most common supercontinent formation, while small and large supercontinents are unlikely to form. The histogram is plotted against the size of supercontinent $Cr = I\,Cr_p$ and the formation number I is labelled on top of each bin.

and 8, although many of the formation numbers are transient (such as $I = 1$ and $I = 8$). The most common and persistent formation number we can visually see in Fig. 13(c) is $I = 4$, and this is confirmed in the histogram of $I(t)$ shown in Fig. 13(d).

In Fig. 13(d), each bin corresponds to the total number of appearances of supercontinents with size I (shown on top of each bin), and the horizontal axis shows the corresponding covering ratio. We indeed see that $I = 4$ plates is the most frequent size of a supercontinent. For small supercontinents, they tend to merge and form a larger but stable supercontinent. For large supercontinents, the random fluid forcing can trigger a disintegration and break it into many smaller ones. Especially for $I \geqslant 6$, our theory predicts such formations are not stable, hence supercontinents with $I \geqslant 6$ are rarely formed and (once formed) are unstable.

The results shown in Fig. 12 and Fig. 13 are common for simulations with different number (N_p) and size (Cr_p) of plates. And we identify $I\,Cr_p < Cr^*$ as a clue for predicting the supercontinental size I.

5. Discussion

Through our numerical investigations, we clearly see the covering ratio as the main factor affecting the thermal blanket effect, which determines the plate dynamics. This is especially apparent during the formation of supercontinents– the continent covering ratio cannot exceed Cr^*, as the strong thermal blanket effect will induce a diverging surface flow that pulls the formed supercontinent apart.

As our current study is inspired by laboratory experiments, we certainly look forward to future experimental investigations of the interaction between multiple plates. Besides the geometry presented in Figs. 1 and 2, the broader investigation of fluid-structure interactions in thermal convection also includes adding fixed obstacles to the convective domain (Bao *et al.* 2015; Li *et al.* 2024), modifying the convective boundary conditions (Zhang *et al.* 2020; Huang & Zhang 2022), and allowing for moving boundaries that are

driven by the fluid forcing (Mercier *et al.* 2014; Wang & Zhang 2023) or phase change (Huang *et al.* 2021; Huang & Moore 2022; Weady *et al.* 2022). Many of these works are certainly geophysically inspired, addressing long-standing mysteries such as the super rotation of Earth's inner core (Wang & Zhang 2023; Yang & Song 2023).

In order to more closely simulate the geophysical plate tectonics, there are several future directions to improve our model. The first one is to investigate the plate tectonics in a 3-dimensional geometry, including the mantle-like spherical shell and the rectangular cuboidal fluid domain that is periodic in two horizontal directions. Pioneer works including Lowman & Gable (1999); Mao *et al.* (2019); Mao (2021) have investigated the fluid-structure interaction and plate interaction in these settings. They also used the geophysical parameters of the mantle, most notably a Prandtl number around 10^{23} (Meyers *et al.* 1987). Incorporating the aforementioned geometry and parameters of the mantle is one future direction for our study.

The interaction between continental plates is also more complicated in geophysical plate tectonics, as the converging continental plates deform the contact region and form the tallest mountains of Earth. It is still an ongoing quest to understand the consequences of converging and diverging continents, with many recent works focusing on the deforming contact region and addressing its influence on the mantle flow beneath (Rozel *et al.* 2017; Whitehead 2023). Inspired by the geophysics, one modification to our current model could be changing the way neighboring plates interact. This can be achieved through changing the coefficient of restitution to 0 during each collision, which better captures the collision between continental plates during a long time scale. Adding an attractive force between plates can also reveal interesting dynamics, as the diverging surface flow has to be strong enough to pull the plates apart. These modifications are awaiting implementation, and they may reveal new insights into the physics and dynamics of the formation of supercontinents.

In our present work, we have fixed the fluid aspect ratio $\Gamma = 4$ in all the numerical examples. We note that Γ can significantly affect the formation of supercontinents. In Huang (2024), the critical covering ratio Cr^* is shown to depend on the aspect ratio as $Cr^* \sim \Gamma^{-2/3}$ when Γ is large. This indicates that the maximum length of a stable supercontinent is $\Gamma Cr^* \sim \Gamma^{1/3}$, so its size increases slowly with increasing Γ.

To conclude, we consider a toy model to predict the size of the largest continental plate. The aspect ratio of Earth's mantle is roughly $\Gamma_E = 10$, so the critical covering ratio there is $Cr_E^* \approx (\Gamma_E/\Gamma)^{-2/3} Cr^* \approx 0.2$ where we have taken $\Gamma = 4$ and $Cr^* = 1/3$ from our study. This gives an estimated dimension of the largest stable continental plate of Earth, $L \approx 2\pi R_E Cr_E^*$, where $R_E = 6400$ km is the radius of Earth. So the plate area is approximately $L^2 \approx 7 \times 10^7$ km^2, slightly underestimating the largest continental plate, the North American Plate, whose area is 7.59×10^7 km^2.

Supplementary Materials

Supplementary movies are available at https://math.nyu.edu/~jinzi/research/convectivePlate-np/Movie.

REFERENCES

AHLERS, G., GROSSMANN, S. & LOHSE, D. 2009 Heat transfer and large scale dynamics in turbulent Rayleigh-Bénard convection. *Rev. Mod. Phys.* **81** (2), 503.

ARAUJO, F. F., GROSSMANN, S. & LOHSE, D. 2005 Wind Reversals in Turbulent Rayleigh-Bénard Convection. *Phys. Rev. Lett.* **95** (8), 084502.

Bao, Y., Chen, J., Liu, B.-F., She, Z.-S., Zhang, J. & Zhou, Q. 2015 Enhanced heat transport in partitioned thermal convection. *Journal of Fluid Mechanics* **784**, R5.

Brown, E. & Ahlers, G. 2007 Large-Scale Circulation Model for Turbulent Rayleigh-Bénard Convection. *Phys. Rev. Lett.* **98** (13), 134501.

Burke, K. 2011 Plate Tectonics, the Wilson Cycle, and Mantle Plumes: Geodynamics from the Top. *Annual Review of Earth and Planetary Sciences* **39** (Volume 39, 2011), 1–29.

Chernih, A., Sloan, I. H. & Womersley, R. S. 2014 Wendland functions with increasing smoothness converge to a Gaussian. *Advances in Computational Mathematics* **40** (1), 185–200.

Elder, J. 1967 Convective self-propulsion of continents. *Nature* **214** (5089), 657–660.

Gurnis, M. 1988 Large-scale mantle convection and the aggregation and dispersal of supercontinents. *Nature* **332** (6166), 695–699.

Hou, T. Y. & Li, R. 2007 Computing nearly singular solutions using pseudo-spectral methods. *Journal of Computational Physics* **226** (1), 379–397.

Howard, L. N., Malkus, W. V. R. & Whitehead, J. A. 1970 Self-convection of floating heat sources: A model for continental drift. *Geophysical and Astrophysical Fluid Dynamics* **1** (1-2), 123–142.

Huang, J. M. 2024 Covering convection with a thermal blanket: numerical simulation and stochastic modelling. *Journal of Fluid Mechanics* **980**, A47.

Huang, J. M. & Moore, N. J. 2022 Morphological attractors in natural convective dissolution. *Physical Review Letters* **128** (2), 024501.

Huang, J. M., Shelley, M. J. & Stein, D. B. 2021 A stable and accurate scheme for solving the Stefan problem coupled with natural convection using the Immersed Boundary Smooth Extension method. *Journal of Computational Physics* **432**, 110162.

Huang, J. M. & Zhang, J. 2022 Rayleigh–Bénard thermal convection perturbed by a horizontal heat flux. *J. Fluid Mech.* **954**.

Huang, J. M., Zhong, J.-Q., Zhang, J. & Mertz, L. 2018 Stochastic dynamics of fluid–structure interaction in turbulent thermal convection. *J. Fluid Mech.* **854**.

Kious, W. J. & Tilling, R. I. 1996 *This dynamic Earth: the story of plate tectonics*. DIANE Publishing.

Li, Y.-Z., Chen, X. & Xi, H.-D. 2024 Enhanced heat transfer and reduced flow reversals in turbulent thermal convection with an obstructed centre. *Journal of Fluid Mechanics* **981**, A16.

Lowenstein, J. H. 2024 Near-critical behavior of the Zhong-Zhang model. *Phys. Rev. E* **109**, 025102.

Lowman, J. P. & Gable, C. W. 1999 Thermal evolution of the mantle following continental aggregation in 3D convection models. *Geophysical Research Letters* **26** (17), 2649–2652.

Lowman, J. P. & Jarvis, G. T. 1993 Mantle convection flow reversals due to continental collisions. *Geophysical Research Letters* **20** (19), 2087–2090.

Lowman, J. P. & Jarvis, G. T. 1995 Mantle convection models of continental collision and breakup incorporating finite thickness plates. *Physics of the Earth and Planetary Interiors* **88** (1), 53–68.

Lowman, J. P. & Jarvis, G. T. 1999 Effects of mantle heat source distribution on supercontinent stability. *Journal of Geophysical Research: Solid Earth* **104** (B6), 12733–12746.

Lowman, J. P., King, S. D. & Gable, C. W. 2001 The influence of tectonic plates on mantle convection patterns, temperature and heat flow. *Geophysical Journal International* **146** (3), 619–636.

Mao, Y. 2021 An insulating plate drifting over a thermally convecting fluid: the effect of plate size on plate motion, coupling modes and flow structure. *Journal of Fluid Mechanics* **916**, A18.

Mao, Y., Zhong, J.-Q. & Zhang, J. 2019 The dynamics of an insulating plate over a thermally convecting fluid and its implication for continent movement over convective mantle. *Journal of Fluid Mechanics* **868**, 286–315.

Mercier, M. J., Ardekani, A. M., Allshouse, M. R., Doyle, B. & Peacock, T. 2014 Self-propulsion of immersed objects via natural bioconvection. *Physical Review Letters* **112** (20), 204501.

MEYERS, R. A. *et al.* 1987 *Encyclopedia of physical science and technology*. Academic Press.

MOORE, N. J. & HUANG, J. M. 2023 Fluid pendulum explains reversals of the large-scale circulation in thermal convection. *arXiv preprint arXiv:2307.13148* .

PEYRET, R. 2002 *Spectral methods for incompressible viscous flow*, , vol. 148. Springer Science & Business Media.

PLUMMER, C. C., McGEARY, D., CARLSON, D. H. *et al.* 2001 *Physical geology*. McGraw-Hill Boston.

ROZEL, A. B., GOLABEK, G. J., JAIN, C., TACKLEY, P. J. & GERYA, T. 2017 Continental crust formation on early Earth controlled by intrusive magmatism. *Nature* **545** (7654), 332–335.

TREFETHEN, L. N. 2000 *Spectral methods in MATLAB*. SIAM.

TURCOTTE, D. L. & SCHUBERT, G. 2002 *Geodynamics*. Cambridge University Press.

WANG, K. & ZHANG, J. 2023 Persistent corotation of the large-scale flow of thermal convection and an immersed free body. *Proceedings of the National Academy of Sciences* **120** (21), e2217705120.

WEADY, S., TONG, J., ZIDOVSKA, A. & RISTROPH, L. 2022 Anomalous Convective Flows Carve Pinnacles and Scallops in Melting Ice. *Phys. Rev. Lett.* **128**, 044502.

WHITEHEAD, J. A. 1972 Moving heaters as a model of continental drift. *Phys. Earth Planet. In.* **5**, 199–212.

WHITEHEAD, J. A. 2023 Convection cells with accumulating crust: models of continent and mantle evolution. *Journal of Geophysical Research: Solid Earth* **128** (4), e2022JB025643.

WHITEHEAD, J. A. & BEHN, M. D. 2015 The continental drift convection cell. *Geophys. Res. Lett.* **42** (11), 4301–4308.

YANG, Y. & SONG, X. 2023 Multidecadal variation of the Earth's inner-core rotation. *Nature Geoscience* **16** (2), 182–187.

ZHANG, J. & LIBCHABER, A. 2000 Periodic boundary motion in thermal turbulence. *Physical Review Letters* **84** (19), 4361.

ZHANG, S., XIA, Z., ZHOU, Q. & CHEN, S. 2020 Controlling flow reversal in two-dimensional Rayleigh–Bénard convection. *Journal of Fluid Mechanics* **891**, R4.

ZHONG, J.-Q. & ZHANG, J. 2005 Thermal convection with a freely moving top boundary. *Phys. Fluids* **17** (11), 115105.

ZHONG, J.-Q. & ZHANG, J. 2007*a* Dynamical states of a mobile heat blanket on a thermally convecting fluid. *Physical Review E* **75** (5), 055301.

ZHONG, J.-Q. & ZHANG, J. 2007*b* Modeling the dynamics of a free boundary on turbulent thermal convection. *Physical Review E* **76** (1), 016307.

ZHONG, S. & GURNIS, M. 1993 Dynamic feedback between a continentlike raft and thermal convection. *Journal of Geophysical Research: Solid Earth* **98** (B7), 12219–12232.

ZHONG, S., ZUBER, M. T., MORESI, L. & GURNIS, M. 2000 Role of temperature-dependent viscosity and surface plates in spherical shell models of mantle convection. *Journal of Geophysical Research: Solid Earth* **105** (B5), 11063–11082.